scientific reports

OPEN

Thirty percent conversion efficiency from radiofrequency power to thrust energy in a magnetic nozzle plasma thruster

Kazunori Takahashi

Innovations for terrestrial transportation technologies, e.g., cars, aircraft, and so on, have driven historical industries so far, and a similar breakthrough is now occurring in space owing to the successful development of electric propulsion devices such as gridded ion and Hall effect thrusters, where solar power is converted into the momentum of the propellant via acceleration of the ionized gases, resulting in a high specific impulse. A magnetic nozzle (MN) radiofrequency (rf) plasma thruster consisting of a low-pressure rf plasma source and a MN is an attractive candidate for a high-power electric propulsion device for spacecraft, as it will provide a long lifetime operation at a high-power level due to the absence of an electrode exposed to the plasma and a high thrust density. The high-density plasma produced in the source is transported along the magnetic field lines toward the open-source exit and the plasma is then spontaneously accelerated in the MN. By ejecting the plasma flow from the system, the reaction forces are exerted to the thruster structure including the source and the MN, and the spacecraft is resultantly propelled. The thruster will open the next door for space technologies, while the performance of the MN rf plasma thruster has been lower than those of the mature electric propulsion devices due to the energy loss to the physical walls. Here the thruster efficiency of about 30%, being the highest to date in this type of thruster, is successfully obtained in the MN rf plasma thruster by locating a cusp magnetic field inside the source, which acts as a virtual magnetic wall isolating the plasma from the source wall. The increase in the thrust by the cusp can be explained by considering the reductions of the loss area and the plasma volume in a thrust analysis combining a global source model and a one-dimensional MN model.

Electric propulsion (EP) is one of the advanced transportation technologies in space and plays an important role in space activities as a spacecraft engine in recent years[1–3]. The gaseous propellant is priorly ionized and the charged particles in the plasmas are energized and accelerated by applying electromagnetic fields. As electric power obtained by solar panels is converted into the kinetic energy of the propellant, the EP devices can provide a high specific impulse, which corresponds to a thrust per unit mass of the propellant, compared with chemical propulsion devices[4]. Representatively, EP devices such as gridded ion and Hall effect thrusters have been successfully used in various space missions, e.g., SMART-1 mission[5], Dawn mission[6], BepiColombo mission[7], and Hayabusa 1 and 2 missions[8,9]. More recently, a new type of gridded ion thrusters utilizing iodine propellant has been successfully operated in orbit[10]. In these types of thrusters, the ions are electrostatically accelerated and exhausted together with the equal flux of the electrons supplied from neutralizers; zero net current exhausted from the system is maintained. When DC electric power is coupled with the plasmas, the electrodes in the thruster and the neutralizer have to be exposed to the plasmas and are often damaged by ion sputtering and thermal load. Therefore, the lifetime of the thruster has been a critical issue and been extended by elaborating designs of the gridded ion and Hall effect thrusters e.g., the 7-kW class NEXT ion thruster has been successfully operated for about 50,000 h on the ground test[11]. The lifetime extension would become a challenging problem when further increasing the operating power.

Some types of electrodeless plasma thrusters have been proposed and under investigation toward high-power, long-lived, and high-thrust-density EP devices, e.g., a variable specific impulse plasma rocket (VASIMR) and a

[1]Department of Electrical Engineering, Tohoku University, Sendai 980-8579, Japan. [2]Interdisciplinary Research Center for Non-equilibrium Plasma, Tohoku University, Sendai 980-8579, Japan. email: kazunori.takahashi.e8@tohoku.ac.jp

MN radiofrequency (rf) plasma thruster, which is sometimes called a helicon thruster. In the former, most of the electric power is coupled with the ions via an ion cyclotron resonance heating (ICRH) and their perpendicular energy is converted into the directed axial energy by a magnetic nozzle (MN), where superconducting magnets are required to apply the strong magnetic fields for the ICRH[12]. For the latter case, most of the rf power is transferred to the electrons via a Joule and/or helicon wave heating processes, providing the high-density plasma production in the source, where the source can be operated with relatively low magnetic fields[13,14]. As the electron temperature is much larger than the ion temperature in the MN rf plasma thrusters, conversion processes from the electron energy to the thrust energy are key issues to improve the thruster performance.

When applying the MN to the rf plasma source, a number of experiments have shown that the electric fields are spontaneously formed and the ions in the high potential source are accelerated toward the low potential side[15]; the energetic electrons overcoming the potential drop neutralize the accelerated ions[16]. These observations have indicated that the MN rf plasma thruster does not require a neutralizer. The role of the spontaneous electrostatic acceleration is the conversion of the electron energy to the ion dynamic energy[17]. During the plasma expansion in the MN, an internal azimuthal plasma current spontaneously develops due to the diamagnetic nature; the axial Lorentz force arising from the diamagnetic current and the radial magnetic field increases the thrust, as predicted and demonstrated by theories and experiments[18–21]. The conversion efficiencies from the rf power to the thrust energy were about 0.5–5% in early experiments[22–26] and approaches about 20% in recent years[27], based on the scientific insights into the thrust generation processes. Some models and experiments have identified that the energy and momentum losses to the source wall yield the low thruster efficiency and the inhibition of the loss by increasing the strength of the axial magnetic fields have been discussed and demonstrated so far[28,29]. The efficiency of the thruster is still lower than the gridded ion and Hall effect thrusters, which is probably due to insufficient inhibition of the plasma loss to the wall; it is crucial to improve the thruster performance step-by-step.

Here we report a 30% conversion efficiency from the rf power to the thrust energy in the MN rf plasma thruster, which is the highest to date, where a cusp magnetic field is formed in the upstream side of the source tube, while maintaining the MN structure downstream of the source. It is clearly observed that the plasma inside the source tube is aligned along the cusp magnetic field; the upstream plasma is geometrically isolated from the source wall, resulting in the inhibition of the plasma loss to the wall and the improvement of the thruster performance. The detected thrust is consistent with the electron diamagnetic Lorentz force estimated from the radial plasma profile. The result is qualitatively explained by an analysis combining a global source model and a one-dimensional MN model, where changes in the effective loss area and the discharge volume are taken into account.

Experimental setup

The schematic of the experimental setup is shown in Fig.1a. The experiment is performed with the MN rf plasma thruster consisting of an 11-cm-outer-diameter, 10.5-cm-inner-diameter, and 25-cm-long glass source tube wound by a double-turn rf loop antenna centered at $z = -13$ cm and two solenoids centered at $z = -3.8 \pm 0.2$ cm and -22.5 ± 0.2 cm, which are labeled as "downstream" and "upstream" solenoids, respectively. The axial position of the right-hand edge of the downstream solenoid holder is defined as $z = 0$ and the open-source exit is set at $z = -1$ cm. The upstream side of the source tube is terminated by an insulator mica back plate. The whole structure of the thruster is attached to a pendulum thrust balance immersed in a 1-m-diameter and 2-m-long vacuum chamber evacuated to a base pressure less than 10^{-4} Pa by three turbomolecular pumping systems. As it has already been reported that the better thruster performance can be obtained when introducing the propellant gas near the open-source exit[30], argon gas is introduced from the ceramic tube located near the thruster exit as seen in Fig.1a. The gas flow rate is maintained at 70 sccm (2.1 mg/s) and the pressure measured at the chamber sidewall is about 28 mPa, which is ten times higher than the standard background pressure recommended for testing gridded ion and Hall effect thrusters. This is due to the limited effective pumping speed (being about 4500 Ls^{-1} for argon), while no detectable change in the thrust of the MN rf plasma thruster has been induced by the different pumping speeds giving the pressures of 28 mPa and 88 mPa[31]. DC solenoid currents I_{Bup} and I_{Bdown} are supplied to the upstream and downstream solenoids by dc power supplies, respectively, for applying the magnetic fields. Each solenoid has a copper wire would around the solenoid holder 638 turns (29 turns and 22 turns in the axial and radial directions). Figure 1b shows the calculated magnetic fields on the z axis for various I_{Bup} and $I_{Bdown} = 22.3$ A, where the positive and negative currents provide the magnetic fields directing rightward and leftward on their centers, respectively. Two-dimensional structures of the magnetic field lines for $(I_{Bup}, I_{Bdown}) = (0, 22.3$ A) and $(-15$ A, 22.3 A) are drawn in Fig. 1c and d, respectively. By supplying the negative current for I_{Bup}, it can be seen that the zero axial magnetic field on the axis, called the cusp magnetic field, is formed inside the source tube. The expanding magnetic field, i.e., the MN, is formed downstream of the source tube, and no drastic change can be seen in the MN region when changing I_{Bup}. The rf loop antenna is powered by a 13.56 MHz rf generator via an impedance matching box, where two variable capacitors in the matching box are tuned in advance to minimize the rf power reflection during the plasma production and no detectable power reflection can be seen for all the data. The plasma produced inside the source and expanding along the MN is visually confirmed.

The axial displacement of the pendulum is induced by the plasma production, which corresponds to the thrust, and is measured by a laser displacement sensor. The detailed procedure can be found in 'Method' section. The absolute value of the thrust is obtained by multiplying a calibration coefficient relating the displacement to the force (see 'Method' section). The thruster efficiency η_T is estimated from the measured thrust F, the mass flow rate of the propellant $\dot{m}$, and the forward rf power P_{rf} as
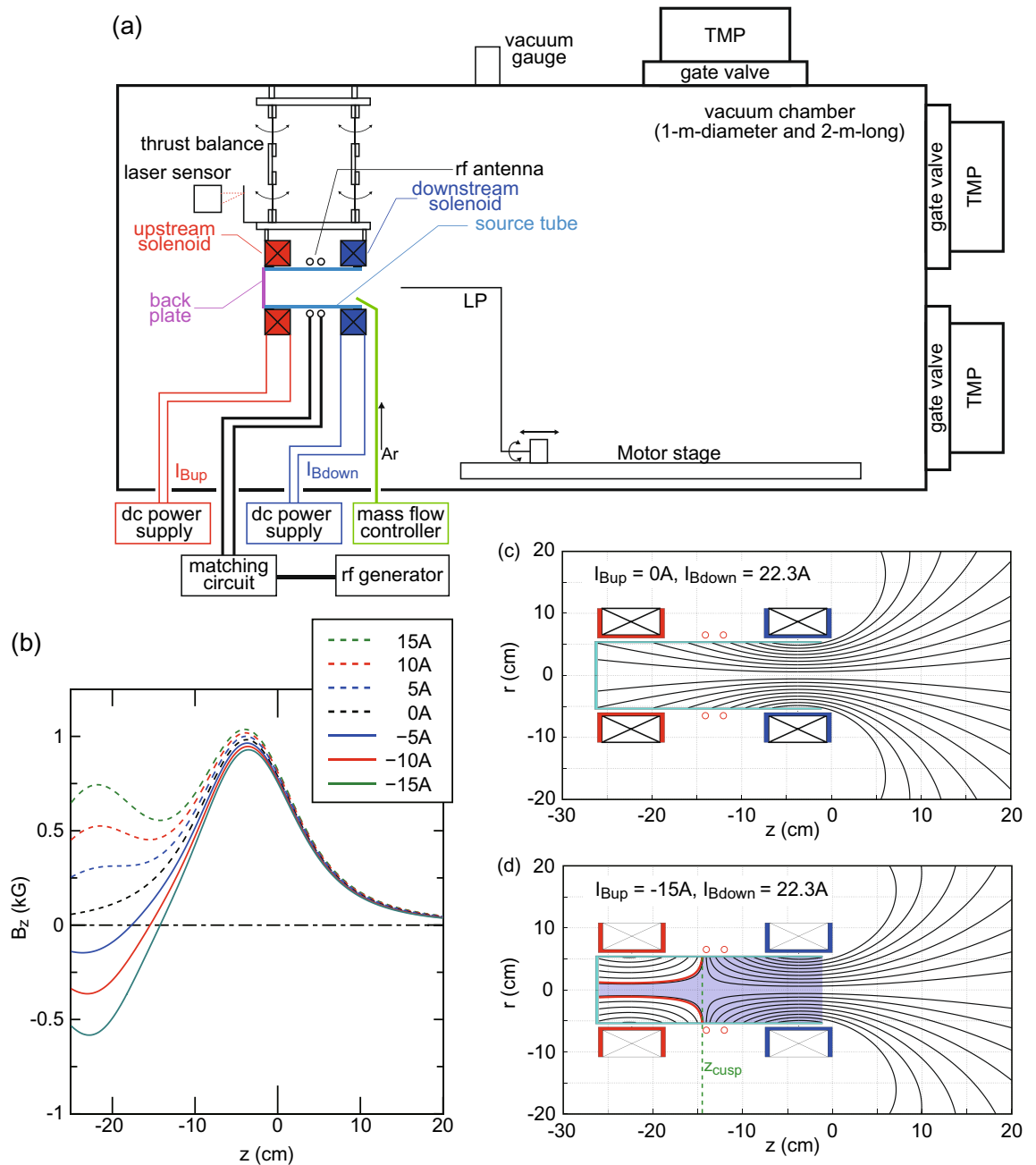
Figure 1. Experimental setup and magnetic field structures. (**a**) Schematic diagram of the experimental setup. (**b**) Calculated magnetic fields B_z on the z axis for various upstream solenoid currents I_{Bup}, where the downstream solenoid current is maintained at $I_{Bdown} = 22.3$ A. The two-dimensional profiles of the magnetic field lines for (**c**) $(I_{Bup}, I_{Bdown}) = (0, 22.3$ A$)$ and (**d**) $(I_{Bup}, I_{Bdown}) = (-15$ A, 22.3 A$)$. The axial position giving the zero magnetic field on the radial center is defined as z_{cusp} as drawn by the dotted line in (**d**). The bold red lines and the blue-colored regions in (**d**) show the field lines intersecting the inner source wall at $z = z_{cusp}$, and the volume for the global model analysis. The cusp is formed for $I_{Bup} < 0$ and the axial position z_{cusp} of the cusp can be shifted by changing I_{Bup}, while no drastic change is seen in the MN region.

$$\eta_T = \frac{F^2}{2\dot{m}P_{rf}}, \tag{1}$$

where the electric power for the solenoids is not taken into account here. Hence η_T indicates the conversion efficiency from the rf power to the thrust energy. Furthermore, the rf power transfer efficiency η_p, which is defined as the ratio of the power absorbed by the plasma to the rf power, is also assessed by measuring the rf antenna current as described in 'Method' section, since it directly affects the plasma production and the resultant thrust generation. A 3-mm-diameter planar Langmuir probe (LP), which radially faces, is mounted on an axially and
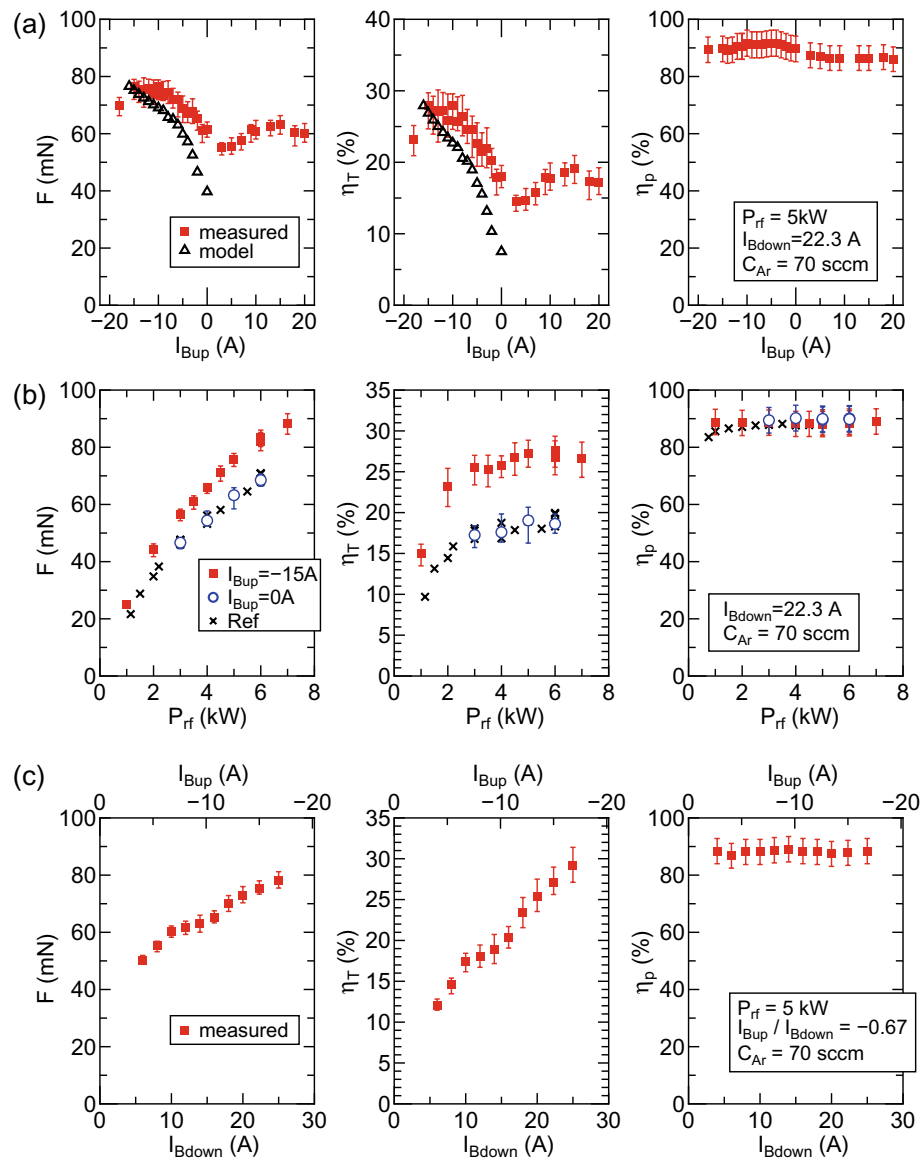
Figure 2. Characterized thruster performance. Measured thrust F, thruster efficiency η_T, and rf power transfer efficiency η_p as functions of (**a**) I_{Bup} for $I_{Bdown} = 22.3$ A (filled red squares), (**b**) P_{rf} for $I_{Bup} = 0$ A (open blue circles) and for $I_{Bup} = -15$ A (filled red squares), and (**c**) I_{Bup} and I_{Bdown} with maintaining the constant ratio of $I_{Bup}/I_{Bdown} = -0.67$ (filled red squares). The data from Ref.[27] is plotted by crosses in (**b**) for comparison. The open black triangles in (**a**) are obtained from the thruster model including the global source model and the one-dimensional MN model, where the changes in the plasma loss area and the volume are considered and $\eta_p = 0.9$ is used for the calculation. The thruster performance (F and η_T) can be increased by forming the cusp in the source ($I_{Bup} < 0$) as in (**a**, **b**) and by increasing the magnetic field strength as in (**c**), while the efficient rf power coupling of $\eta_p \sim 90\%$ is maintained for all the conditions. The maximum thruster efficiency of $\eta_T \sim 30\%$ is successfully obtained. The increase in the thrust can be qualitatively explained by the model as in Fig.1a.

radially movable motor stage. The ion saturation current I_{is} of the negatively biased LP is measured, which is given by $I_{is} = 0.61en_pu_BS$ with the elementary charge e, the plasma density n_p, the Bohm velocity u_B, and the detection area S of the LP. Typical electron temperature measured at $(r, z) = (0, 10$ cm$)$ is about 6 ± 1 eV; the plasma density for $I_{is} = 1$ mA can be roughly estimated as $3.8 \pm 0.5 \times 10^{17}$ m^{-3}/mA. As the Bohm velocity is given by $u_B = (k_BT_e/m_i)^{1/2}$ with the Boltzmann constant k_B, the electron temperature T_e, and the ion mass m_i, I_{is} is proportional to $n_pT_e^{1/2}$, being a rough indicator of the electron pressure ($p_e = n_pk_BT_e$) with an error of $T_e^{1/2}$.

Results and discussion

Filled red squares in Fig. 2a show the measured thrust F, the thruster efficiency η_T, and the rf power transfer efficiency η_p as functions of I_{Bup} for $P_{rf} = 5$ kW and $I_{Bdown} = 22.3$ A. F and η_T slightly increase for $I_{Bup} = 10$ -15 A, which would be due to the increase in the magnetic field strength inside the source (see Fig.1b) and the

resultant inhibition of the plasma loss to the source wall as reported in Ref.[29]. Very interestingly, the significant increases in F and η_T can be obtained for $I_{Bup} < 0$ with the cusp inside the source, in spite of the decreases in the source field strength as shown in Fig. 1b. The thruster efficiency of about $\eta_T \sim 27.5\%$ can be obtained in the range of $-15\,A \leq I_{Bup} \leq -10\,A$.

F, η_T, and η_p as functions of P_{rf} are assessed when powering only the downstream solenoid, i.e., $(I_{Bup}, I_{Bdown}) = (0, 22.3\,A)$, as plotted by open blue circles in Fig. 2b, and compared with the previous experiment (crosses)[27]. It should be noted that $I_{Bdown} = 22.3\,A$ can provide the peak magnetic field strength being close to the previous experiment[27]. The differences between the open blue circles and crosses are only the source tube materials and sizes (10.5-cm-inner-diameter and 25-cm-long glass tube and 9.5-cm-inner-diameter and 20-cm-long ceramic tube for the present and previous experiments, respectively); the similar values of F, η_T, and η_p are obtained. Red filled squares in Fig. 2b show the results for $(I_{Bup}, I_{Bdown}) = (-15\,A, 22.3\,A)$, indicating the performance improvement by forming the cusp inside the source over the rf power range tested here. Only the magnetic field strength can be controlled with the unchanged spatial structure of the magnetic field lines by changing both I_{Bup} and I_{Bdown} while maintaining I_{Bup}/I_{Bdown} at a constant level. Figure 2c shows F, η_T, and η_p as functions of I_{Bup} and I_{Bdown} under the condition of $I_{Bup}/I_{Bdown} = -0.67$. F and η_T continuously increases with the increase in the field strength, being consistent with the earlier experiment[20]. For the maximum field strength case of $(I_{Bup}, I_{Bdown}) = (-16.8\,A, 25\,A)$, the thruster efficiency of $\eta_T \sim 30\%$, being the highest to date, can be successfully obtained. It is noted that η_p is about 90% for all the data in Fig. 2. The measured total resistance R_{total} including the antenna (R_{vac}) and plasma (R_p) resistances ranges from 4.5 to 6 Ω, while the antenna resistance is about 0.56 Ω. Since the condition of $R_{total} \gg R_{vac}$ is maintained for all the conditions, the parametric change in R_{total} within the range of 4.5–6.5 Ω does not significantly affect η_p. This fact shows that the power absorbed by the plasma is unchanged by the external parameters in the present experiment and implies that the enhanced thrust is not due to the change in the rf power coupling but due to the presence of the cusp.

To understand the effect of the cusp, two-dimensional profiles of the ion saturation current I_{is} are taken and shown in Fig. 3 for $(I_{Bup}, I_{Bdown}) = $ (a) $(0\,A, 22.3\,A)$, (b) $(-10\,A, 22.3\,A)$, and (c) $(-15\,A, 22.3\,A)$. The plasma follows the magnetic field lines and contact with the radial source wall upstream of the rf antenna for the no cusp case as in Fig.3a. When the cusp is formed inside the source as in Fig. 3b and c, the nearly zero density is observed in the peripheral region upstream of the cusp and the plasma is geometrically isolated from the wall. This effectively decreases the plasma loss area to the wall and the discharge volume, whose effect will be incorporated in the simple model described later. It is noted that the off-axis density peak appears inside the source and transported along the magnetic field lines as clearly seen in Fig. 3b and c. Such a structure has been observed in a number of experiments and discussed with the electron heating by the rf electromagnetic fields[32–36]; 2-D simulations of wave-plasma interactions have shown the off-axis profile of the rf electromagnetic fields[37,38]. The off-axis density peak is also reproduced in a 2-D particle-in-cell simulations[39,40]. Furthermore, a 2D simulation with the cusp in the source have been performed more recently[41], showing the off-axis density profile and the reduction of the density near the wall upstream of the cusp.

The previous studies have shown that the Lorentz force due to the electron diamagnetic current and the radial magnetic field in the MN increases the thrust and is the major component of the total thrust. The local Lorentz force f_{De} is then described as[20]

$$f_{De} = -\frac{B_r}{B_z}\frac{\partial p_e}{\partial r} \propto -\frac{B_r}{B_z}\frac{\partial I_{is}}{\partial r}, \tag{2}$$

where the ion saturation current I_{is} is assumed to be proportional to the electron pressure. Figure 4a shows the radial profile of I_{is} taken at $z = 5$ cm as a function of I_{Bup}, indicating the center-peaked and annular profiles for $I_{Bup} > 0$ and $I_{Bup} < 0$, respectively. Figure 4b shows the local Lorentz force f_{De} calculated by Eq. (2) with the measured I_{is} and the calculated magnetic fields. It can be found that the Lorentz force is generated near the plasma edge where the pressure gradient is large. Assuming the axisymmetric profile of f_{De}, the Lorentz force ΔF_{De} integrated over the cross section is plotted by open circles in Fig. 4c, together with the measured thrust F, where the error bar for ΔF_{De} originates from the asymmetry between $r > 0$ and $r < 0$ in Fig. 4b. Since the calculated ΔF_{De} can qualitatively explain the variation in the thrust as seen here, it can be deduced that the increase in the Lorentz force contributes to the performance improvement. It should be noted that the actual thrust component due to the Lorentz force in the MN is obtained by the volume integration; only the qualitative discussion can be made by using ΔF_{De}.

For further understanding of the cusp effect on the thruster performance, the changes in the plasma loss area and the volume are incorporated into a global source model connected to a one-dimensional MN model. The details of the model are described in 'Method' section. Briefly, the electron temperature T_e and the plasma density n_s in the source region are assumed to be uniform; the particle and power balance equations are numerically solved. As observed in Fig. 3b and c, the plasma is geometrically isolated from the source wall by the cusp, resulting in the reduction of the loss area and the discharge volume. It is assumed that the plasma upstream of the cusp is confined within the magnetic field lines (bold red lines in Fig. 1d) intersecting the inner source wall at $z = z_{cusp}$, where z_{cusp} is the axial position giving the zero magnetic field on the radial center. It is assumed that the loss area is the back and radial walls where the plasma contacts and the discharge volume is the blue-colored region as shown in Fig. 1d. Substituting the plasma density and electron temperature in the source into the one-dimensional MN model and the flux conservation law, the axial profiles of the velocity and density can be obtained. Then the total thrust can be calculated from these physical quantities inside the source and in the MN. It should be emphasized again that the model can be used only to qualitatively explain the increase in the thrust by the cusp, since the loss area corresponding to the wall where the plasma contacts and the plasma volume do not significantly change for $I_{Bup} > 0$.
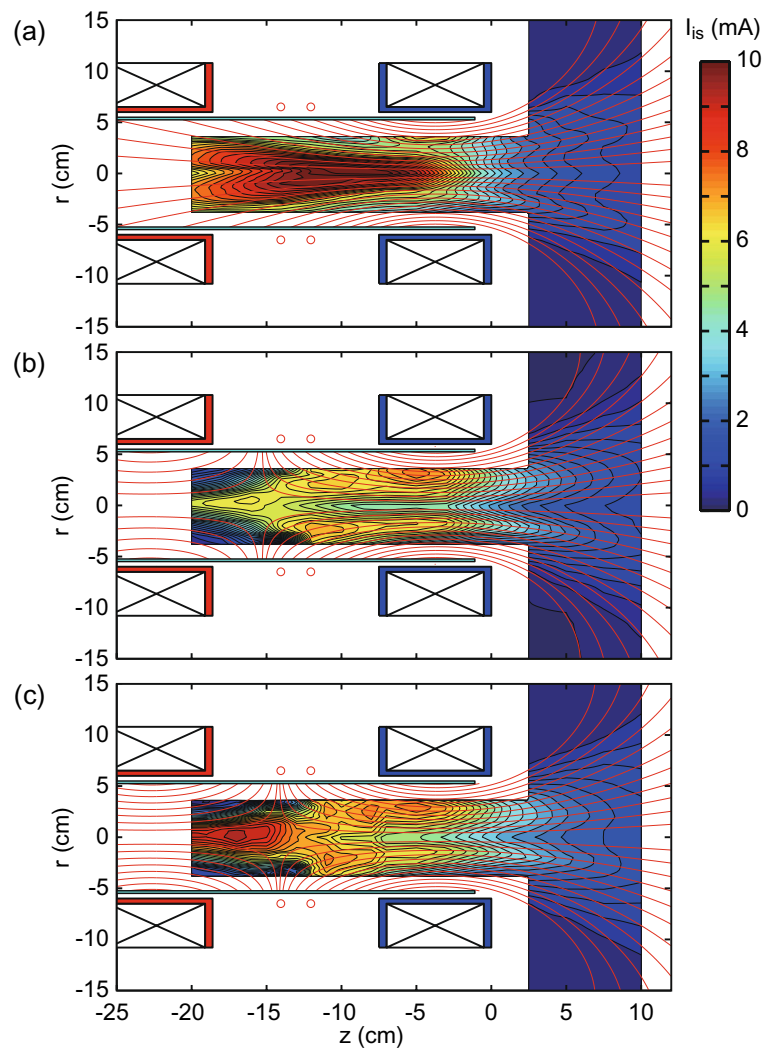
Figure 3. Two-dimensional plasma mapping inside the source. Two-dimensional profiles of the ion saturation current I_{is} of the LP, which roughly mirrors the electron pressure profiles, for (**a**) $I_{Bup} = 0$ A, (**b**) $I_{Bup} = -10$ A, and (**c**) $I_{Bup} = -15$ A, together with the calculated magnetic field lines, where the downstream solenoid current and the rf power are maintained at $I_{Bdown} = 22.3$ A and $P_{rf} = 5$ kW, respectively. The profiles roughly follow the magnetic field lines for all the cases. Especially, it can be found that the ion current close to zero is observed at the peripheral region upstream of the rf antenna as in (**b**, **c**). The presence of the cusp provides the geometric isolation of the plasma from the source wall.

Figure 5a shows n_s and T_e in the source as a function of I_{Bup}, where the axial position z_{cusp} of the cusp is shifted by I_{Bup}, implying that the source density can be increased by supplying the larger negative current I_{Bup} to the upstream solenoid, i.e., by forming the cusp closer to the rf antenna. In this calculation, the rf power transfer efficiency is maintained at $\eta_p = 0.9$ as observed in Fig.2a. Figure 5b shows the typical axial profiles of the ion Mach number M and the plasma density n_p in the MN; it shows the ion acceleration and the density decay along the MN. The total thrust, i.e., the axial momentum flux, is found to increase along the MN, where the finally obtained thrust would correspond to T_{total} at the axial position where the plasma detachment occurs. As the plasma detachment is still an open question[42–46], T_{total} at $z = 50$ cm is used for discussion. The calculated T_{total} at $z = 50$ cm and the thruster efficiency η_T are plotted by open triangles in Fig. 2a, where the analysis is performed only for $I_{Bup} < 0$ as no cusp reducing the loss area and the plasma volume is formed for $I_{Bup} > 0$. It is found that the model qualitatively explains the performance improvement for $I_{Bup} < 0$, i.e., by the cusp. This indicates that the cusp acts as the virtual wall isolating the plasma from the source wall and reducing the particle and energy losses to the physical walls.

As already described before, the thruster assessments have been performed with various designs and parameters; typical performance data from literature are summarized in Table 1. Figure 6 shows the thruster efficiency η_T calculated from the measured thrust F, the rf power P_{rf}, and the mass flow rate $\dot{m}$ of the propellant, as a function of F/P_{rf}. The performance data in Table 1 are plotted by open circles in Fig. 6 with the number corresponding to the indexes labeled by the publication column in Table 1. The present data showing the maximum efficiency
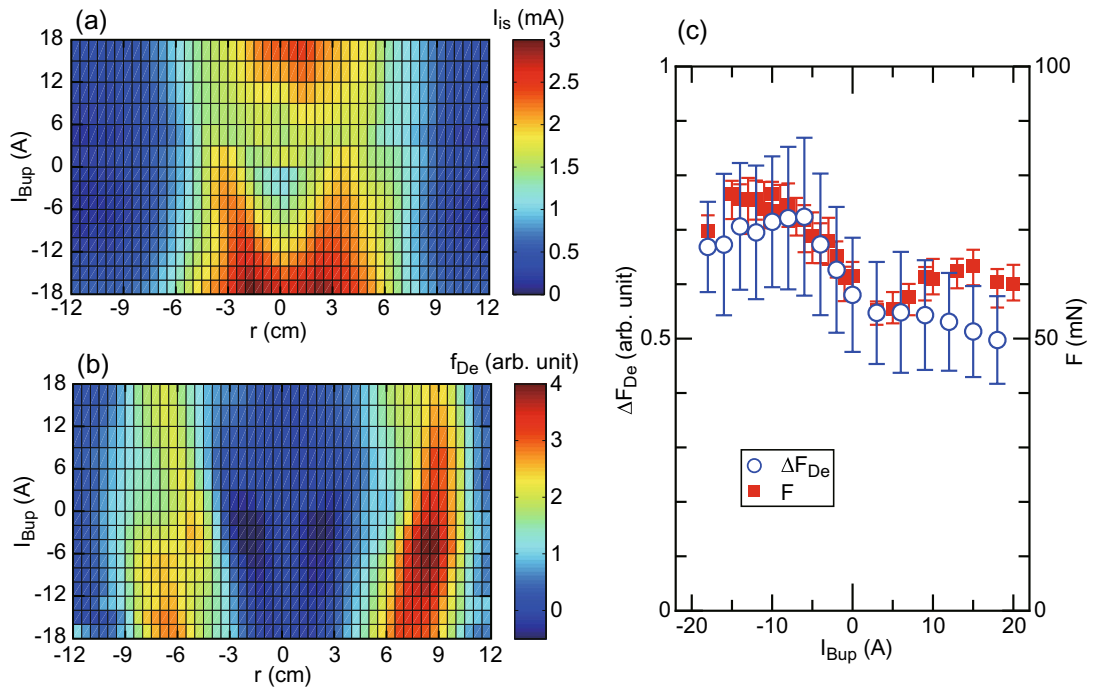
Figure 4. Qualitative estimation of the Lorentz force in the MN. Radial profiles of (**a**) the ion saturation current I_{is} of the LP taken at $z = 5$ cm and (**b**) the relative value of the local electron-diamagnetic Lorentz force f_{De} calculated from the measured I_{is} and the calculated magnetic fields. (**c**) The Lorentz force $\Delta F_{De} = 2\pi \int_0^r r f_{De} dr$ integrated over the cross section (blue open circles), together with the measured thrust F (filled red squares, same data as Fig. 2a).
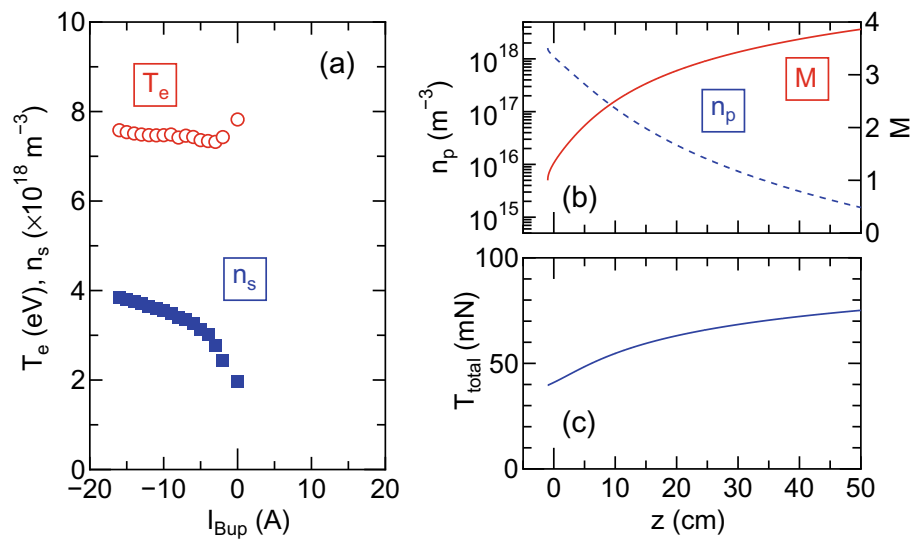

Figure 5. The results from the global source model and the one-dimensional MN model. (**a**) The plasma density n_s (blue filled squares) and electron temperature T_e (red open circles) in the source, as a function of I_{Bup}. Typical axial profiles of (**b**) the ion Mach number M, the plasma density n_p, and (**c**) the thrust T_{total}. The increase in the source plasma density for $I_{Bup} < 0$ can be seen. The velocity increases and the plasma density decays along the MN. The increase in T_{total} along the MN is confirmed. As the finally obtained thrust would depend on the axial location of the plasma detachment, which is still an open question, T_{total} at $z = 50$ cm is used for discussion and is plotted by open triangles in Fig. 2a.

Publications	P_{rf} (kW)	F (mN)	F/P_{rf} (mN/kW)	η (%)
1-Takahashi et al. APL2011[23]	0.9	3	3.3	0.83
2-Pottinger et al. JPD2011[22]	0.65	2.8	4.3	0.6
3-Takahashi et al. PRL2011[47]	0.8	6	7.5	3.0
4-Charles et al. APL2012[48]	0.8	5	6.3	2.1
5-Takahashi et al. PRL2013[20]	1	11	11.0	8.4
6-Shabshelowitz and Gallimore JPP2013[24]	1.5	11	7.33	0.58
7-Williams and Walker JPP2013[25]	0.6	6	10	0.67
8-Takahashi et al. JPD2013[49]	2	15	7.5	7.8
9-Charles et al. APL2013[50]	0.9	6	6.7	2.3
10-Harle et al. PSST2013[51]	0.4	1.1	2.75	0.25
11-Takahashi et al. PSST2014[52]	2	20	10	13.3
12-Takahashi et al. PSST2015[53]	6	58	9.7	13.3
13-Kuwahara et al. JPP2017[54]	3	40	13.3	3.0
14-Oshio et al. IEPC2017[55]	1	6	6.0	1.5
15-Trezzolani et al. IEPC2017[56]	0.15	1.4	9.33	3.3
16-Trezzolani et al. IEPC2017[57]	0.07	0.85	12.1	5.2
17-Takahashi et al. JPP2020[58]	1	25	25	7.1
18-Navarro-Cavallé et al. IEPC2019[59]	0.45	8.5	18.9	14.2
19-Takahashi et al. SciRep2021[27]	6	69.63	11.6	19.24

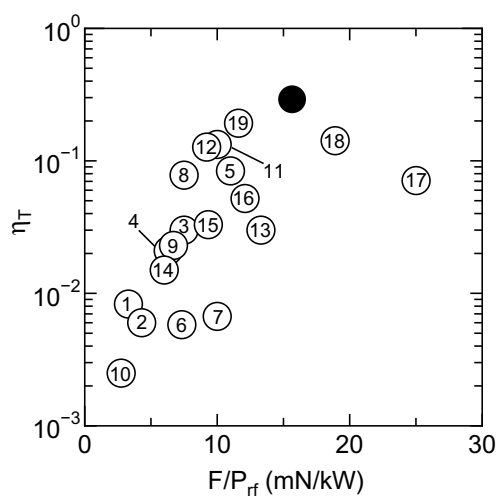**Table 1.** Performances of the MN rf plasma thrusters from the literature.

Figure 6. Thruster performances from literature and the present experiment. Thruster efficiency η_T versus F/P_{rf} from the published literature (open circles with the number corresponding to the indexes of the publication column in Table 1) and the present data showing the maximum efficiency (a black filled circle). This clearly shows the increase in the thruster efficiency compared with the previous studies.

is also plotted by a filled circle in Fig. 6, clearly indicating the increase in the thruster efficiency by the presence of the cusp inside the source tube.

It should be noted again that the thruster efficiency is calculated from the rf power P_{rf} from the rf generator; hence it does not take the solenoid power and the power loss at the rf generator into account. The solenoids can be partially replaced by permanent magnets as investigated in previous studies[60–62]. Furthermore, developments of rf systems for the thrusters have also been progressed such as efficient switching-type rf generators[63,64] and compact frequency-tunable impedance matching techniques[65,66]. The system developments providing less power losses at the solenoids and the rf generator, reducing the system size, and improving the controllability, remains further challenging issues toward a flight model of the MN rf plasma thruster.

Even if no electrode is exposed to the plasmas, the insulator source wall will be sputtered when the energy of the ions impinging the wall exceeds the threshold of the sputtering as being a crucial problem in the Hall effect thrusters, where the accelerated ions having an energy close to the discharge voltage would be the major factor
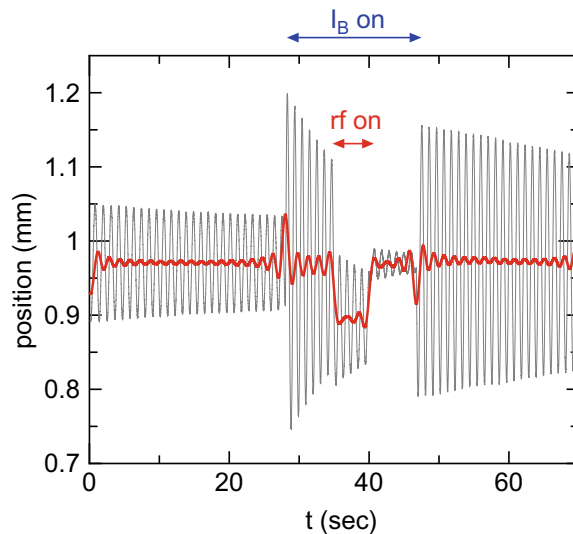
Figure 7. Thrust measurement procedure. Typical raw signal from the laser displacement sensor (a gray thin line), where the solenoid currents and the rf power are turned on for $t \sim 25 - -47$ s and $t \sim 35 - -40$ s, respectively. A red bold line shows the filtered signal for minimizing the amplitude of the pendulum oscillation and for estimation of the equilibrium positions for tuning on only the solenoid currents ($t \sim 27 - -35$ s) and for turning on both the solenoid currents and the rf power ($t \sim 35 - -40$ s).

for the wall erosion[67]. The ions impinging the source wall in the MN rf plasma thruster is only accelerated by a sheath at the wall, which has a voltage of about $5.2T_e$ for argon[68]. As discussed by Del Valle et al., the threshold energy of the sputtering for a quartz glass, being about 35 eV, is close to the typical sheath voltage in the low-pressure rf discharge[69]. Therefore, the wall erosion induced by the sputtering will be minimized by choosing the wall materials properly and by reducing the electron temperature near the wall (i.e., the sheath voltage). The lifetime of the MN rf plasma thruster has not been verified yet and remains further development issue.

Conclusion

The thruster efficiency estimated from the measured thrust, the rf power, and the mass flow rate of the propellant, is successfully increased up to about thirty percent by forming the cusp magnetic field at the upstream region of the source. It is demonstrated that the cusp field geometrically isolates the plasma from the source wall, resulting in the increases of the thrust and the thruster efficiency. The performance improvement can be qualitatively understood by considering the reductions of the plasma loss area and the discharge volume inside the source, where the thruster analysis is made by combining the global source model and the one-dimensional magnetic nozzle model. The presently reported thruster efficiency is the highest to date in this type of thruster called the helicon thruster; the present results would lead to a new transportation technology in space, i.e., the high-power and long-lived electric propulsion device.

Methods

Thrust measurement procedure. Argon gas is continuously introduced into the thruster in advance. A gray line in Fig. 7 shows the raw signal from the laser displacement sensor, which contains the specific oscillation frequency of about 1 Hz due to the pendulum motion. The measured signal is converted into an amplitude spectrum by a Fast Fourier transform and filtered in the frequency domain. The filtered amplitude spectrum is converted into the temporal signal via a Inverse Fast Fourier transform as drawn by a red line in Fig. 7, minimizing the oscillation component of the pendulum.

After confirming a stable equilibrium position of the thrust balance ($t \sim 0$–27 s), both the solenoid currents (I_{Bup} and I_{Bdown}) are simultaneously turned on (at $t \sim 27$ s in Fig. 7), where a rapid increase in the amplitude of the pendulum motion and slight change in the equilibrium position can be seen for $t \sim 27$–35 s due to the inductions of the eddy current on the metallic materials and a magnetic force on magnetic materials (e.g., SUS304). At $t \sim 35$ s, the rf power is turned on for about 5 s, clearly showing the change in the equilibrium position for $t \sim 35$–40 s by the plasma production. The laser sensor signal gets back to the value at $t \sim 27$–35 s after turning off the rf power ($t \sim 40$–47 s) and back to the initial equilibrium position after turning off the solenoid currents ($t > 47$ s). The difference in the equilibrium positions for $t \sim 27$–35 s (turning on only the solenoid currents) and $t \sim 35$–40 s (turning on both the solenoid currents and the rf power) gives the displacement induced only by the plasma production, which does not contain the displacements induced by applying the magnetic field and by injecting the gas. The absolute value of the thrust can be obtained by multiplying the calibration coefficient described in the next section. Since the rf power is turned on only for 5 s in the present experiment, no significant thermal drift has been seen as in Fig. 7.
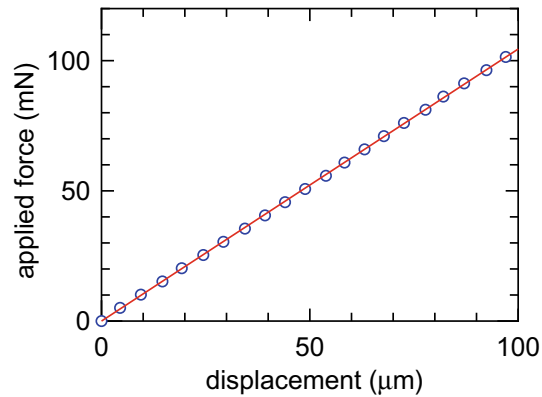
Figure 8. Thrust balance calibration. Measured displacement (blue open circles) versus applied force, together with a fitted linear line (a red solid line) giving the calibration coefficient.

Thrust balance calibration.   Before pumping down the vacuum chamber, a calibration procedure is performed by applying known axial forces to the thruster attached to the balance and measuring the displacement. The measured displacement as a function of the applied force is plotted by blue open circles in Fig. 8. The linearity is well maintained over the force of less than 100 mN at least; the characteristic can be fitted by a linear line as drawn by a red sold line in Fig. 8. The fitted line gives the calibration coefficient as ~ 1.045 mN/μm. It is confirmed that the coefficient is unchanged after performing the experiment and venting the chamber.

RF power transfer efficiency.   The rf power transfer efficiency η_p is defined as a ratio of the rf power absorbed by the plasma to the total rf power. A well-known equivalent circuit model is used here to estimate η_p [70]. Assuming that the input rf power is dissipated by the plasma resistance R_p and the rf antenna resistance R_{vac}, the power transfer efficiency η_p can be given by

$$\eta_p = \frac{R_p}{R_{total}} = \frac{R_{total} - R_{vac}}{R_{total}}, \tag{3}$$

where R_{total} is the total resistance during the plasma production. These resistances can be estimated by measuring the rf antenna current by locating a Rogowski-type current sensor that can be used up to a frequency of 20 MHz (Pearson Electronics, Model 5046) and the net power of the rf generator, which simply corresponds to the forward power minus the reflected power. The antenna resistance of $R_{vac} \sim 0.56 \, \Omega$ is obtained via the same procedure with no gas injection and no plasmas. Since the rf antenna, the rf feedthrough, and the circuit components in the matching box, are water-cooled at a constant temperature of 20 degrees C, the antenna resistance R_{vac} is unchanged during the experiment.

Thruster model.   An analysis combining a global source model and a one-dimensional MN model, which is used for the analyses of the open triangles in Fig. 2a and the data in Fig. 5, is described here. The plasma density n_s and the electron temperature T_e in the source are modeled from the power and particle balance equations in the global model assuming uniform profiles [68]. The balance equation between the particle generation by the ionization process and the loss from the system is given as

$$K_{iz} n_s n_g V = n_s u_B A_{eff}, \tag{4}$$

where K_{iz}, n_g, V, and A_{eff} are the ionization rate constant, the neutral density, the plasma volume, and effective plasma loss area, respectively. The description of A_{eff} and the approximated expression of K_{iz} can be found in Ref. [68] with the radial (h_R) and axial (h_L) center-to-edge density ratios. By numerically solving Eq. (4), the electron temperature T_e can be obtained for the given gas pressure and the source geometry. The power balance between the input energy and the energy lost from the system is given as

$$\eta_p(P_{rf} - P_{ref}) = e n_s A_{eff} u_B E_T, \tag{5}$$

where P_{rf} and P_{ref} are the forward and reflected rf powers, respectively. In the present experiment, the reflected power P_{ref} is undetectable for all the data. E_T is the energy loss due to collisional processes and electron-ion pairs escaping from the system and can be written by

$$E_T = E_i + E_e + E_c, \tag{6}$$

$$E_i = 5.2 T_e \text{ (for argon)}, \tag{7}$$

$$E_e = 2 T_e, \tag{8}$$

$$E_c = E_{iz} + \frac{K_{exc}}{K_{iz}} E_{exc} + 3 \frac{m_e}{m_i} \frac{K_{el}}{K_{iz}} T_e, \tag{9}$$

where E_i, E_e, E_c, E_{iz}, and E_{exc} are the ion kinetic energy loss, the electron kinetic energy loss, the collisional energy loss, the ionization energy, and the excitation energy, respectively. In the calculation, the approximated expression of the ionization (K_{iz}), excitation (K_{exc}), and elastic scattering (K_{el}) rate constants, which are functions of the electron temperature T_e, are used[68]. Substituting T_e obtained from Eq. (4) into Eq. (5), n_s can be numerically calculated for a given neutral density. Although the propellant gas is introduced near the thruster exit in the present experiments, the simple gas model is considered here. When the gas is introduced into the source at a constant mass flow rate $\dot{m}$, the local neutral density n_g can be estimated from $\dot{m} = m_g n_g v_g A_s$, where m_g, v_g, and A_s are the neutral mass, the neutral velocity (assumed to be 400 ms^{-1}), and the cross section of the source tube, respectively.

As already mentioned in the 'Results and discussion' section, the upstream plasma is geometrically isolated from the source wall when applying the cusp magnetic field, resulting in the reductions of the wall area where the plasma contacts and the plasma volume are effectively reduced. This is geometrically estimated from the magnetic field line intersecting the source inner wall at $z = z_{cusp}$ as drawn by the bold red lines and the blue-colored region in Fig. 1d, where the plasma is assumed to be confined within the bold red lines in the upstream region. These effects are taken into account by modifying the effective loss area A_{eff} and the plasma volume V in Eq. (4, 5), where A_{eff} corresponds to the area of the wall to which the plasma (the blue-colored region) contacts, and V is obtained by calculating the volume of the blue-colored region. As plotted in Fig. 5, the plasma density in the source increases for $I_{Bup} < 0$ cases with the increase in $|I_{Bup}|$.

Once n_s and T_e in the source are obtained, the results are substituted into the one-dimensional MN model[71]. Briefly, the thrust is given by the sum of the electron pressure in the source and the Lorentz force exerted on the MN as

$$T_{total} = n_s k_B T_e A_s - - \int_0^z \frac{n_p k_B T_e A}{B_z} \frac{\partial B_z}{\partial z'} dz', \tag{10}$$

where the axial momentum lost to the radial wall, which has been detected when the plasmas are significantly lost to the wall[72], does not appear in the one-dimensional model and A_s is the cross section of the source. The axial velocity of the ions can be given by a similar expression with the physical nozzle model as

$$\frac{M^2 - M_i^2}{2} - \ln\left(\frac{M}{M_i}\right) = \ln\left(\frac{B_{zi}}{B_z}\right), \tag{11}$$

where M is the ion Mach number and the subscript i denotes the value to the MN entrance. To connect the global source model and the MN model, the plasma density and the ion Mach number at the MN entrance (i.e., at the open-source exit) are assumed to be $h_L n_s$ and $M_i = 1$, respectively. The assumption of $M_i = 1$ at the source exit and the MN entrance, which corresponds to an energy of half an electron temperature, requires a density decay by a factor of $\exp(-1/2) \sim 0.6$ according to the Boltzmann relation. This can be briefly validated by the density profiles in Fig. 3. Furthermore, a number of experiments have shown the appearance of the supersonic ions near the source exit[14,15]. The local plasma density n_p in the MN can be given from the particle flux conservation along the MN and the magnetic flux conservation as[71,73]

$$n_p M u_B A = h_L n_s M_i u_B A_s, \tag{12}$$

$$B_z A = B_{zi} A_s. \tag{13}$$

By numerically solving Eqs. (4–13), the source plasma density n_s, the electron temperature T_e, the local plasma density n_p, the ion Mach number M, and the total thrust T_{total} can be obtained. It is noted that the inner diameter (10.5 cm) and length (25 cm) of the source tube installed in the present experiment are used for all the calculation.

Data availability
The data that support the figures within this paper are available from corresponding author upon reasonable request.

References
1. Mozouffre, S. Electric propulsion for satellites and spacecraft: Established technologies and novel approaches. *Plasma Sources Sci. Technol.* **25**, 033002 (2016).
2. Levchenko, I. *et al.* Recent progress and perspectives of space electric propulsion systems based on smart nanomaterials. *Nat. Commun.* **9**, 879 (2018).
3. Levchenko, I. *et al.* Space micropropulsion systems for Cubesats and small satellites: From proximate targets to furthermost frontiers. *Appl. Phys. Rev.* **5**, 011104 (2018).
4. Goebel, D. M. & Katz, I. *Fundamentals electric propulsion: Ion and Hall thrusters* (Wiley, 2008).
5. Foing, B. H. *et al.* SMART-1 mission to the moon: Status, first results and goals. *Adv. Space Res.* **37**, 6 (2006).
6. Brophy, J. The Dawn ion propulsion system. In *The Dawn Mission to Minor Planets 4 Vesta and 1 Ceres* (eds Russell, C. & Raymond, C.) (Springer, 2012).

7. Steiger, C., Montagnon, E., Accomazzo, A. & Ferri, P. BepiColombo mission to Mercury: First year of flight. *Acta Astronaut.* **170**, 472 (2020).
8. Kuninaka, H. *et al.* Powered flight of electron cyclotron resonance ion engines on Hayabusa Explorer. *J. Propul. Power* **23**, 544 (2007).
9. Nishiyama, K., Hosoda, S., Tsukizaki, R. & Kuninaka, H. In-flight operation of the Hayabusa2 ion engine system on its way to rendezvous with asteroid 162173 Ryugu. *Acta Astronaut.* **166**, 69 (2020).
10. Rafalskyi, D. *et al.* In-orbit demonstration of an iodine electric propulsion system. *Nature* **599**, 411 (2021).
11. https://www.nasa.gov/content/next-provides-lasting-propulsion-and-high-speeds-for-deep-space-missions.
12. Bering, E. A. *et al.* Electromagnetic ion cyclotron resonance heating in the VASIMR. *Adv. Space Res.* **42**, 192 (2008).
13. Charles, C. Plasmas for spacecraft propulsion. *J. Phys. D* **42**, 163001 (2009).
14. Takahashi, K. Helicon-type radiofrequency plasma thrusters and magnetic plasma nozzles. *Rev. Mod. Plasma Phys.* **3**, 3 (2019).
15. Charles, C. A review of recent laboratory double layer experiments. *Plasma Sources Sci. Technol.* **16**, R1 (2007).
16. Takahashi, K., Charles, C., Boswell, R. W. & Fujiwara, T. Electron energy distribution of a current-free double layer: Druyvesteyn theory and experiments. *Phys. Rev. Lett.* **107**, 035002 (2011).
17. Fruchtman, A. Electric field in a double layer and the imparted momentum. *Phys. Rev. Lett.* **96**, 065002 (2006).
18. Ahedo, E. & Merino, M. Two-dimensional supersonic plasma acceleration in a magnetic nozzle. *Phys. Plasmas* **17**, 073501 (2010).
19. Takahashi, K., Lafleur, T., Charles, C., Alexander, P. & Boswell, R. W. Electron diamagnetic effect on axial force in an expanding plasma: experiments and theory. *Phys. Rev. Lett.* **107**, 235001 (2011).
20. Takahashi, K., Charles, C. & Boswell, R. W. Approaching the theoretical limit of diamagnetic-induced momentum in a rapidly diverging magnetic nozzle. *Phys. Rev. Lett.* **110**, 195003 (2013).
21. Merino, M. & Ahedo, E. Effect of the plasma-induced magnetic field on a magnetic nozzle. *Phys. Plasmas* **25**, 045012 (2016).
22. Pottinger, S., Lappas, V., Charles, C. & Boswell, R. Performance characterization of a helicon double layer thruster using direct thrust measurements. *J. Phys. D* **44**, 235201 (2011).
23. Takahashi, K. *et al.* Direct thrust measurement of a permanent magnet helicon double layer thruster. *Appl. Phys. Lett.* **98**, 141503 (2011).
24. Shabshelowitz, A. & Gallimore, A. D. Performance and probe measurements of a radio-frequency plasma thruster. *J. Propul. Power* **29**, 919 (2013).
25. Williams, L. T. & Walker, M. L. R. Thrust measurements of a radio frequency plasma source. *J. Propul. Power* **29**, 520 (2013).
26. Furukawa, T., Yarita, Y., Aoyagi, H. & Nishida, H. Measurement of plasma flow and electron energy probability function in radio frequency plasma thruster with a magnetic cusp. *J. Appl. Phys.* **131**, 173302 (2022).
27. Takahashi, K. Magnetic nozzle radiofrequency plasma thruster approaching twenty percent thruster efficiency. *Sci. Rep.* **11**, 2768 (2021).
28. Lafleur, T. Helicon plasma thruster discharge model. *Phys. Plasmas* **21**, 043507 (2014).
29. Takahashi, K., Sugawara, T. & Ando, A. Spatially- and vector-resolved momentum flux lost to a wall in a magnetic nozzle rf plasma thruster. *Sci. Rep.* **10**, 1061 (2020).
30. Takahashi, K., Takao, Y. & Ando, A. Modifications of plasma density profiles and thrust by neutral injection in a helicon plasma thruster. *Appl. Phys. Lett.* **109**, 194101 (2016).
31. Takahashi, K., Takao, Y. & Ando, A. Low-magnetic-field enhancement of thrust imparted by a stepped-diameter and downstream-gas-injected rf plasma thruster. *Plasma Sources Sci. Technol.* **28**, 085014 (2019).
32. Takahashi, K., Charles, C., Boswell, R., Cox, W. & Hatakeyama, R. Transport of energetic electrons in a magnetically expanding helicon double layer plasma. *Appl. Phys. Lett.* **94**, 191503 (2009).
33. Charles, C. High density conics in a magnetically expanding helicon plasma. *Appl. Phys. Lett.* **96**, 051502 (2010).
34. Ghosh, S. *et al.* Formation of annular plasma downstream by magnetic aperture in the helicon experimental device. *Phys. Plasmas* **24**, 020703 (2017).
35. Gulbrandsen, N. & Fredriksen, Å. RFEA measurements of high-energy electrons in a helicon plasma device with expanding magnetic field. *Front. Phys.* **5**, 2 (2017).
36. Takahashi, K., Akahoshi, H., Charles, C., Boswell, R. W. & Ando, A. High temperature electrons exhausted from rf plasma sources along a magnetic nozzle. *Phys. Plasmas* **24**, 084503 (2017).
37. Tian, B., Merino, M. & Ahedo, E. Two-dimensional plasma-wave interaction in an helicon plasma thruster with magnetic nozzle. *Plasma Sources Sci. Technol.* **27**, 114003 (2018).
38. Jiménez, B., Merino, M. & Ahedo, E. Wave propagation and absorption in a helicon plasma thruster and its plume. *Plasma Sources Sci. Technol.* **31**, 045009 (2022).
39. Singh, N., Rao, S. & Ranganath, P. Waves generated in the plasma plume of helicon magnetic nozzle. *Phys. Plasmas* **20**, 032111 (2013).
40. Emoto, K., Takahashi, K. & Takao, Y. Axial momentum gains of ions and electrons in magnetic nozzle acceleration. *Plasma Sources Sci. Technol.* **30**, 115016 (2021).
41. Ma, X., Nishida, H., Oshio, Y. & Furukawa, T. Numerical analysis of RF discharge in a nonuniform magnetic field. *J. Appl. Phys.* **131**, 083302 (2022).
42. Arefiev, A. V. & Breizman, B. N. Magnetohydrodynamic scenario of plasma detachment in a magnetic nozzle. *Phys. Plasmas* **12**, 043504 (2005).
43. Merino, M. & Ahedo, E. Plasma detachment in a propulsive magnetic nozzle via ion demagnetization. *Plasma Sources Sci. Technol.* **23**, 032001 (2014).
44. Olsen, C. S. *et al.* Investigation of plasma detachment from a magnetic nozzle in the plume of the VX-200 magnetoplasma thruster. *IEEE Trans. Plasma Sci.* **43**, 252 (2015).
45. Takahashi, K. & Ando, A. Laboratory observation of a plasma-flow-state transition from diverging to stretching a magnetic nozzle. *Phys. Rev. Lett.* **118**, 225002 (2017).
46. Little, J. M. & Choueiri, E. Y. Electron demagnetization in a magnetically expanding plasma. *Phys. Rev. Lett.* **123**, 145001 (2019).
47. Takahashi, K., Lafleur, K., Charles, C., Alexander, P. & Boswell, R. W. Electron diamagnetic effect on axial force in an expanding plasma: experiments and theory. *Phys. Rev. Lett.* **107**, 235001 (2011).
48. Charles, C., Takahashi, K. & Boswell, R. W. Axial force imparted by a conical radiofrequency magneto-plasma thruster. *Appl. Phys. Lett.* **100**, 113504 (2012).
49. Takahashi, K., Charles, C., Boswell, R. & Ando, A. Performance improvement of a permanent magnet helicon plasma thruster. *J. Phys. D* **46**, 352001 (2013).
50. Charles, C., Boswell, R. & Takahashi, K. Boltzmann expansion in a radiofrequency conical helicon thruster operating in xenon and argon. *Appl. Phys. Lett.* **102**, 223510 (2013).
51. Harle, T., Pottinger, S. J. & Lappas, V. J. Helicon double layer thruster operation in a low magnetic field mode. *Plasma Sources Sci. Technol.* **22**, 015015 (2013).
52. Takahashi, K., Charles, C., Boswell, R. & Ando, A. Effect of magnetic and physical nozzles on plasma thruster performance. *Plasma Sources Sci. Technol.* **23**, 044004 (2014).
53. Takahashi, K., Komuro, A. & Ando, A. Effect of source diameter on helicon plasma thruster performance and its high power operation. *Plasma Sources Sci. Technol.* **24**, 055004 (2015).

54. Kuwahara, D., Shinohara, S. & Yano, K. Thrust characteristics of high-density helicon plasma using argon and xenon gases. *J. Propl. Power* **33**, 420 (2017).
55. Oshio, Y., Shimada, T. & Nishida, H. Experimental investigation of thrust performance on position relationship between RF antenna and magnetic cusp of RF plasma thruster. in *Proceedings of the 35th International Electric Propulsion Conference*, IEPC-2017-344 (2017).
56. Trezzolani, F. *et al.* Development and test of an high power RF plasma thruster in project SAPERE-STRONG. in *Proceedings of the 35th International Electric Propulsion Conference*, IEPC-2017-462 (2017).
57. Trezzolani, F. *et al.* Development and testing of a miniature helicon plasma thruster. in *Proceedings of the 35th International Electric Propulsion Conference*, IEPC-2017-519 (2017).
58. Takahashi, K., Takao, Y. & Ando, A. Increased thrust-to-power ratio of a stepped-diameter helicon plasma thruster with krypton propellant. *J. Propul. Power* **36**, 961 (2020).
59. Navarro-Cavallé, J. *et al.* Development and characterization of the helicon plasma thruster prototype HPT05M. in *Proceedings of the 36th International Electric Propulsion Conference*, IEPC-2019-596 (2019).
60. Takahashi, K., Shida, Y. & Fujiwara, T. Magnetic-field-induced enhancement of ion beam energy in a magnetically expanding plasma using permanent magnets. *Plasma Sources Sci. Technol.* **19**, 025004 (2010).
61. Virko, V. F., Virko, Y. V., Slobodyan, V. M. & Shamrai, K. P. The effect of magnetic configuration on ion acceleration from a compact helicon source with permanent magnets. *Plasma Sources Sci. Technol.* **19**, 015004 (2010).
62. Chen, F. F. A compact permanent-magnet helicon thruster. *IEEE Trans. Plasma Sci.* **43**, 195 (2015).
63. Ziemba, T. *et al.* Plasma characteristics of a high power helicon discharge. *Plasma Sources Sci. Technol.* **15**, 517 (2006).
64. Liang, W. *et al.* An integrated RF power delivery and plasma micro-thruster system for nano-satellites. *Front. Phys.* **6**, 115 (2018).
65. Charles, C., Boswell, R. W. & Bish, A. Variable frequency matching to a radiofrequency source immersed in vacuum. *J. Phys. D* **46**, 365203 (2013).
66. Takahashi, K., Imai, R. & Hanaoka, K. Automatically controlled frequency-tunable rf plasma thruster: Ion beam and thrust measurements. *Front. Phys.* **9**, 639010 (2021).
67. Brown, N. P. & Walker, M. L. R. Review of plasma-induced Hall thruster erosion. *Appl. Sci.* **10**, 3775 (2020).
68. Lieberman, M. A. & Lichtenberg, A. J. *Principles of Plasma Discharges and Materials Processing* 2nd edn. (Wiley, 2005).
69. Del Valle, J. I., Chang Diaz, F. R. & Granados, V. H. Plasma-surface interactions with helicon plasma sources. *Front. Phys.* **10**, 856221 (2022).
70. Lafleur, T., Charles, C. & Boswell, R. W. Characterization of a helicon plasma source in low diverging magnetic fields. *J. Phys. D* **44**, 055202 (2011).
71. Fruchtman, A., Takahashi, K., Charles, C. & Boswell, R. W. A magnetic nozzle calculation of the force on a plasma. *Phys. Plasmas* **19**, 033507 (2012).
72. Takahashi, K., Chiba, A., Komuro, A. & Ando, A. Axial momentum lost to a lateral wall of a helicon plasma source. *Phys. Rev. Lett.* **114**, 195001 (2015).
73. Smolyakov, A. I., Sabo, A., Yushmanov, P. & Putvinskii, S. On quasineutral plasma flow in the magnetic nozzle. *Phys. Plasmas* **28**, 060701 (2021).

Acknowledgements

Author contributions

K.T. designed the experiments, took and analyzed the data, and wrote the manuscript.

Competing interests

The author declares no competing interests.

Additional information

Correspondence and requests for materials should be addressed to K.T.

Reprints and permissions information is available at www.nature.com/reprints.

Publisher's note Springer Nature remains neutral with regard to jurisdictional claims in published maps and institutional affiliations.